

Structure and Infrastructure Engineering

Maintenance, Management, Life-Cycle Design and Performance

ISSN: (Print) (Online) Journal homepage: <https://www.tandfonline.com/loi/nsie20>

Effect of pinching on structural resilience: performance of reinforced concrete and timber structures under repeated cycles

Angelo Aloisio, Matteo Pellicciari, Alessandro Vittorio Bergami, Rocco Alaggio,
Bruno Briseghella & Massimo Fragiaco

To cite this article: Angelo Aloisio, Matteo Pellicciari, Alessandro Vittorio Bergami, Rocco Alaggio, Bruno Briseghella & Massimo Fragiaco (2022): Effect of pinching on structural resilience: performance of reinforced concrete and timber structures under repeated cycles, Structure and Infrastructure Engineering, DOI: [10.1080/15732479.2022.2053551](https://doi.org/10.1080/15732479.2022.2053551)

To link to this article: <https://doi.org/10.1080/15732479.2022.2053551>



Published online: 26 Mar 2022.



Submit your article to this journal [↗](#)




View related articles [↗](#)



View Crossmark data [↗](#)



Effect of pinching on structural resilience: performance of reinforced concrete and timber structures under repeated cycles

Angelo Aloisio^a , Matteo Pelliciaro^b, Alessandro Vittorio Bergami^c, Rocco Alaggio^c, Bruno Briseghella^d and Massimo Fragiaco^d

^aDepartment of Civil, Construction-Architecture and Environmental Engineering, Università degli Studi dell'Aquila, L'Aquila, Italy;

^bDepartment of Civil and Environmental Engineering, Università degli Studi di Modena e Reggio Emilia, Modena, Italy; ^cEngineering Department, University of Roma Tre, Rome, Italy; ^dCollege of Civil Engineering, Fuzhou University, Fuzhou, PR China

ABSTRACT

This article attempts to define pinching of two structural joints, reinforced concrete (RC) and wood ones. In particular, the research outlines differences and analogies between pinching of an RC portal and a Light Timber Frame (LTF) wall. This is done by focusing on the concavity of pinching in their response under repeated cycles, which produces differences in the energy dissipation. The response of the two structural archetypes under pseudo-static and dynamic simulations is analysed using the Atan hysteresis model modification. The truncated incremental dynamic analysis (TIDA) of the two systems modelled as single-degree-of-freedom (SDOF) oscillators yielded the fragility curves, approximated by a lognormal cumulative distribution (CDF). The stability of RC under repeated cycles reveals its significant resilience compared to LTF structures. The examination of the fragility functions supports a discussion about the relation between the pinching concavity and the notion of structural resilience by introducing a robustness index ranging from 0 to 1. Ultimately, a parametric analysis of a fictitious structural system derived from the timber one by varying the concavity of the pinching path leads to the estimation of the robustness index as a function of the pinching concavity.

ARTICLE HISTORY

Received 30 July 2021

Revised 18 December 2021

Accepted 25 January 2022

KEYWORDS

Resilience; pinching; hysteresis modelling; reliability analysis

1. Introduction

This research examines the relationship between pinching and structural resilience by considering the quasi-static and seismic performance of reinforced concrete (RC) and timber archetypes under repeated cycles. The effect of pinching affects the response of structural systems under multiple high-amplitude oscillations. Therefore, repeated earthquakes can highlight the impact of diverse pinching on structural performance.

The repetition of a seismic event leads to a damage accumulation dependent on the progression and typology of degradation. Repeated earthquakes can represent an actual situation, i.e. seismic sequences distinguished by the repetition of medium-strong earthquake ground motions after short intervals. In such cases, the structure, already damaged after the first earthquake and not yet repaired, may become wholly inadequate at the end of the seismic sequence. Several scholars noticed that the seismic behaviour after repeated cycles depends on damage accumulation related to the type of hysteresis (Amadio, Fragiaco, & Rajgelj, 2003; Fragiaco, Amadio, & Macorini, 2004) and the nature of the seismic event (Raghunandan & Liel, 2013). Most of researches (Elnashai, Bommer, & Martinez-Pereira, 1998; Faisal, Majid, & Hatzigeorgiou, 2013; Hatzigeorgiou & Beskos, 2009). Zhai et al. (2014) focused on ductility demand after repeated cycles, by addressing the role of

ductility and degradation on the performance after multiple cycles (Hosseinpour & Abdelnaby, 2017).

However, there are numerous contributes about the main-shock after-shock performance of steel (Abdollahzadeh, Mohammadgholipour, & Omranian, 2019; Abdollahzadeh & Sadeghi, 2018), RC (Jamnani, Amiri, & Rajabnejad, 2018; Salami, Kashani, & Goda, 2019) and masonry (Casolo, 2017; Mouyiannou, Penna, Rota, Graziotti, & Magenes, 2014) buildings, while a fewer about timber structures (Luo, He, Chen, & Li, 2021; Qin & Chouw, 2017). So far, there is no research that investigates the role of diverse pinching on structural resilience. Structural resilience is the system capacity to lessen the consequences of a shock, absorb the shock if it occurs, and recover quickly after it (Bruneau & Reinhorn, 2006). Accordingly, the response of a structural system under repeated earthquakes is related to structural resilience. Additionally, no scholar compared the performance of RC and timber structures under repeated cycles, neither highlighted the consequences of pinching on structural resilience.

Resilience is a broad concept. For example, in civil engineering, it is the system capacity to reduce the consequences of a shock, absorb the shock if it occurs, and recover quickly after it. Thus, a resilient system should have reduced failure probabilities, reduced consequences from failures, and

reduced recovery time. In this research, it is addressed the notion of structural robustness, which concur with and it is part of structural resilience. Robustness expresses the capacity to endure a given level of stress or demand without experiencing degradation or loss of function.

This research addresses the lack of literature about the degradation of structures due to pinching and has the following objectives:

- quantifying analogies and differences of the pinching behaviour in RC and timber structures.
- identification of a synthetic parameter representative of the pinching effect.
- estimation of the seismic performance of an elementary timber archetype *via* nonlinear dynamic analyses under repeated earthquakes using an empirical hysteresis model calibrated on the experimental data;
- defining a probability-based robustness indicator, which expresses the consequences of repeated cycles.
- analysis of the effect of variable pinching that is fictitiously obtained by varying the curvature of the pinching path of the reference experimental hysteresis curve;
- discussion of the consequences of variable pinching on resilience of timber structures.

2. Definition of pinching

Although numerous scholars dedicated their research efforts to developing hysteresis models with pinching and degradation, to the best of authors' knowledge, no scholar attempted to provide a general definition of pinching in structural systems. In ordinary language, the term *pinching* identifies localised deformation. In structural engineering, pinching identifies the local plasticisation due to the mutual compression of two elements. It occurs when a pinching element induces local plasticisation in a pinched one. However, a proper definition of pinching should derive from the distinction between pinching's act and effect. The act of pinching descends from the mutual penetration between two elements, the pinching element against the pinched one. The effect of pinching generally originates from the nature of the pinched element and its reaction to localised stress.

In timber structures, pinching's main drawback is a reduced stiffness after the first load cycle and an abrupt stiffness boost before attaining the maximum displacement achieved in the first cycle (Guíñez, Santa María, & Almazán, 2019; Jorissen & Fragiaco, 2011). The metal connector determines the local failure of the timber element during the first load cycle. Accordingly, the pinching element encounters little resistance during the re-loading phase. However, the wood fibres, despite having lost mechanical strength, retain resistance to penetration. The penetrated fibres compact and grow in stiffness as the deformation increases. When the deformation equals that occurred in the precedent cycle, the phenomenon of local plasticisation progresses, including additional materials.

In RC structures, the effect of pinching may be less evident but still determining (Mitra, 2007; Sengupta & Li, 2016). The RC element cracks due to the attainment of a specific deformation. The inner crack becomes the pinching site: the fracture surface, highly irregular due to the concrete's heterogeneity, pinches the other fracture surface. The angular nature of the surface causes a diffuse pinching action in correspondence with the penetration areas. Differently from timber, the effect of re-loading does not cause an initial stiffness reduction followed by a sudden stiffness increment. In RC elements, the result of pinching manifests as a general stiffness reduction up to the attainment of the deformation level achieved in the previous cycle (Bojórquez et al., 2017; Kostinakis & Athanatopoulou, 2016; Modica & Stafford, 2014; Ozcebe & Saatcioglu, 1989; Park, Kent, and Sampson, 1972).

Therefore, it could be improper distinguishing the stiffness boost from that of reduced stiffness after the first loading cycle, as stated by Porcu (2017). The so-called slip-lock effect (Baber & Noori, 1985) features pinching in timber components but not in RC ones (Favvata & Karayannis, 2014). Wan, Loh, and Peng (2001) and Mansour and Hsu (2005) identify pinching in RC with shear cracking and bond slip of the reinforcement during cyclic loading. Besides, several hysteresis models identify the notion of pinching with a stiffness reduction after the first loading (Aloisio, Alaggio, Köhler, & Fragiaco, 2020; Foliente, 1995; Folz & Filiatrault, 2001). This ambiguity depends on definitions based on the pinching effect on a specific structural system.

Figure 1 anticipates the different effects of pinching in RC and timber structures, mainly manifesting in the opposite concavity of the re-loading paths. The effect of pinching relies on the nature of the pinching and pinched materials. Still, a definition cannot be based on the single act of pinching since its effects make the phenomenon recognisable. Therefore, it is proposed the following definition possibly valuable in structural engineering: *pinching is the act of penetration between a pinching and a pinched element. The possible effect of local damage due to the act of pinching manifests in a reduced stiffness after the first load cycle.* The article discusses similarities and analogies between pinching in timber and RC base joints. Their diverse response to the act of pinching has several implications in earthquake engineering. It is attempted to understand the main consequences of a diverse pinching by focusing on the pseudo-static and dynamic response of two structural archetypes. The two archetypes have equivalent resistance and ductility. However, the effect of distinct pinching generates a different structural response, especially under repeated cycles.

3. Pinching in reinforced concrete and timber joints

Two structural archetypes are examined. The two structural systems, shown in Figure 2, are considered as general representatives of RC and timber structures whose response includes pinching effects. The left picture in Figure 2 is an RC portal, and the right one is a partially-anchored light-

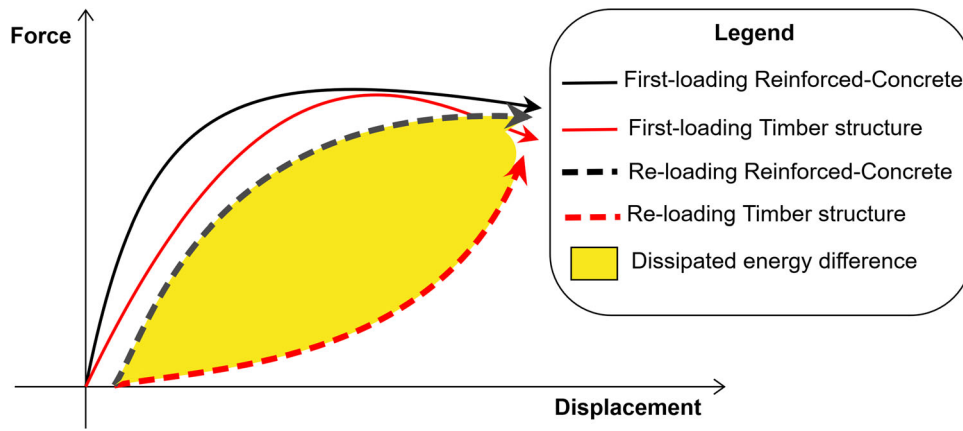


Figure 1. Illustration of the difference in pinching effect between RC and timber structures.

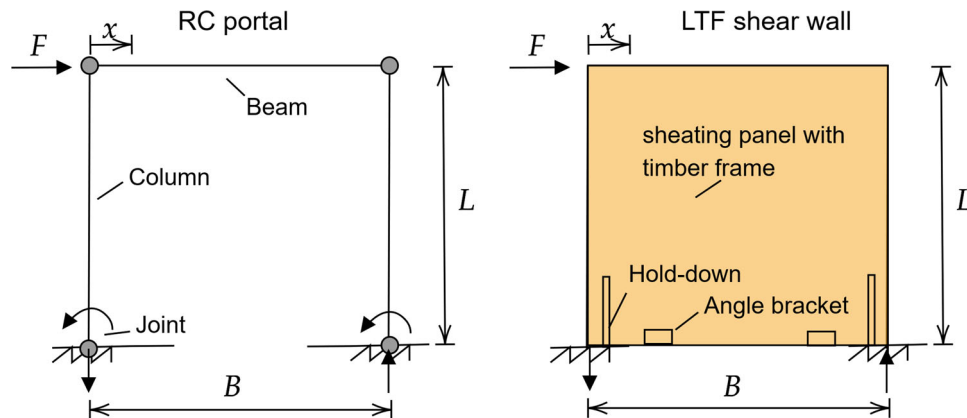


Figure 2. Schematic illustration of an RC portal and a partially-anchored light-timber frame (LTF).

timber frame (LTF) shear wall. The primary resisting mechanism of the RC portal relies upon the moment resistance of the base joints. The leading resistance mechanism of the LTF shear wall depends on the hold-down failures. In both structures, the ultimate resistance is localised at the base joints, the RC base joints and the hold-downs, respectively. Despite the inherent differences, the dissipation capacity arises from the hysteretic response of the base joints.

Both systems are known to reveal the effects of pinching. However, although both archetypes manifest a stiffness reduction after the first load cycle, the diversity in the re-loading paths' concavity may lead to diverse seismic performances. The following paragraphs shortly report on the experimental cyclic response of two structural systems with similar displacement and force capacity, corresponding to the ones in Figure 2: an RC portal tested by Bergami and Nuti (2015) and an LTF shear wall tested by Grossi, Sartori, and Tomasi (2015).

3.1. Reinforced concrete portal

Bergami and Nuti (2015) executed experimental cyclic tests on a bare RC portal, with executive draw reported in Figure 3. The experimenters imposed a cyclic displacement on the top of the portal. The loading protocol in Figure 4(a) had the following characteristics: magnitude of the first cycle 1 mm (± 0.5 mm); three cycles for each magnitude step;

magnitude increases by ± 0.5 mm up to the achievement of the maximum strength and subsequent increments ± 1.0 mm; cycles with a constant frequency of 0.05 Hz.

The first plastic hinges manifested by the base joints, associated with a 4.33 mm imposed displacement (0.17% inter-story drift). The progression of damage mainly invested the base joints. In correspondence with an 8.63 mm top displacement, additional cracks arose in the beam-column joints (0.34% inter-story drift). When the top displacement exceeded 15 mm (0.6% inter-story drift), the rebars buckling at the base joints induced the concrete expulsion. When the portal was approaching collapse, further concrete fragments were expelled from the inner side of the beam-column joints.

Figure 4 reports the experimental cyclic response in terms of force-displacement, force-time and dissipated energy-time functions. Interestingly, most of the damage and dissipation is localised by the base joints. Therefore, the shape of the hysteresis curve chiefly originates from the base joints response, responsible for the evident reduction in stiffness after the first load cycles.

3.2. LTF shear wall

Grossi et al. (2015) executed experimental cyclic tests on several LTF shear walls. The specimen characterised by an ultimate resistance that is the most similar to that of the RC

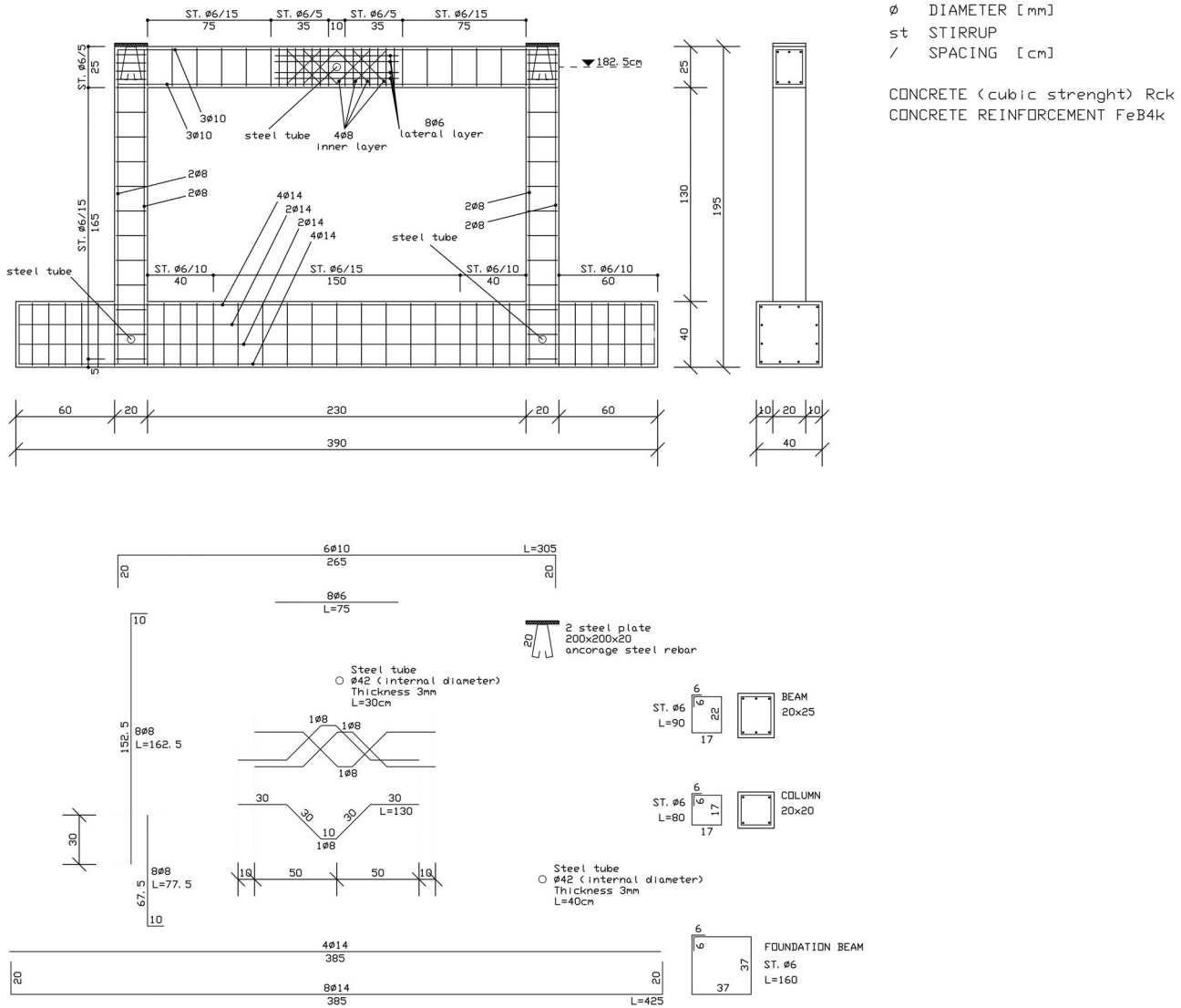


Figure 3. Executive draw of the RC portal tested by Bergami et al. (2015).

specimen is selected. The chosen sample has OBS sheathing and nails as fasteners. The panel has two WHT620 hold-downs fastened by 52 Anker nails. Full details about the specimen and the setup are given in Grossi et al. (2015).

The experimenters carried out a displacement-driven test following the EN 594:2011 protocol of Figure 6(a) imposed on the top of the panel. Figure 6 reports the force-displacement, force-time and dissipated energy-time functions. The force values are measured by the top of the wall. As remarked by Aloisio, Boggian, Roberto, and Fragiaco (2021), the lateral capacity depends on the hold-down resistance. The specimen mainly exhibits a rocking response, while the panel deformation and sliding represent a small fraction of the top displacement, approximately equal to 25%. Accordingly, the panel behaves like a rigid lever that transfers the load to the hold-downs. A capacity model based on the sole hold-down reactions, neglecting the timber compression and the angle brackets reactions, lead to an excellent estimation of the ultimate resistance with a relative error less than 10%.

Therefore, the hysteretic response observed in Figure 6 mostly originates from the pull-out hysteresis of the hold-

downs. The stiffness reduction after the first load cycle depends on pinching between the hold-downs' nails and timber. The two structural archetypes' descriptions prelude the following discussion about the mutual analogies and differences.

4. Differences and analogies

Table 1 compares the performance of the RC and LTF structures in terms of ultimate resistance, yielding and ultimate displacement, and ductility. Although the two structural systems have a similar force and displacement capacity, the energy dissipated by the RC structures is approximately 3.25 higher than the LTF shear wall (see Figure 7(b)).

The difference in the dissipated energy mostly depends on the loading protocol and the different ductility. Specifically, the RC portal's one presents more cycles than the ones recommended by EN 594:2011 for timber structures. However, the direct inspection of the hysteresis loops in Figure 7(a) reveals that the re-loading curves are far

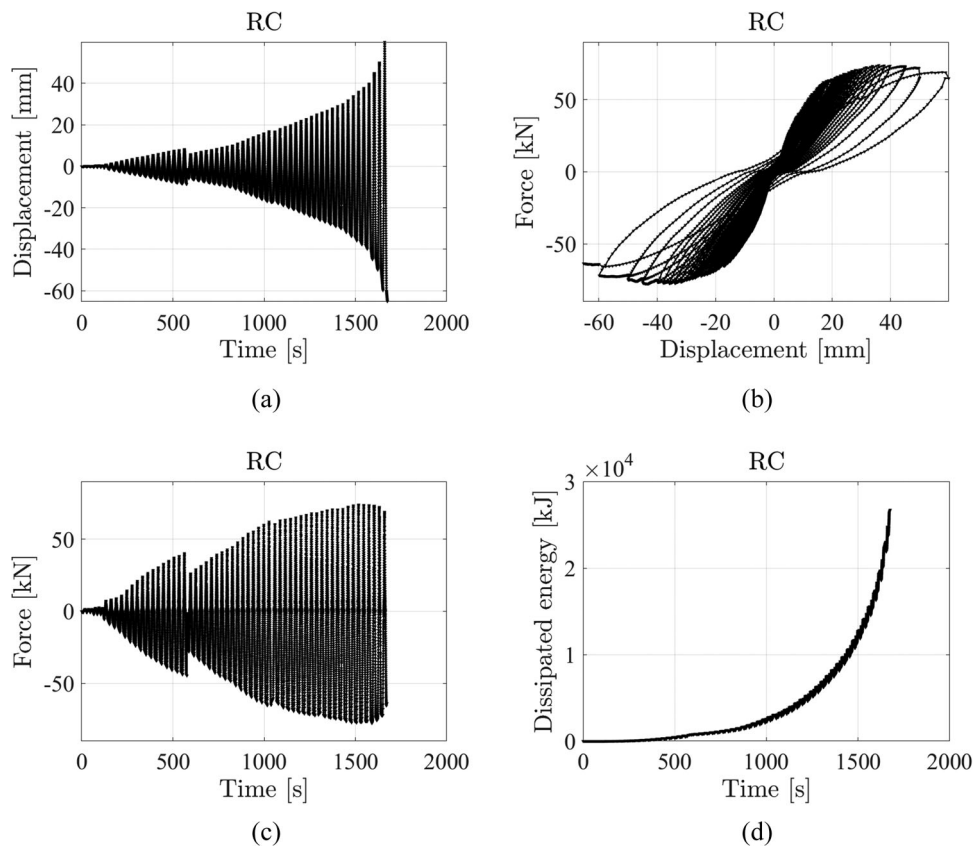


Figure 4. (a) Displacement protocol, (b) hysteresis loop, (c) force-time and (d) dissipated energy-time functions of the RC portal under cyclic loading (Bergami et al., 2015).

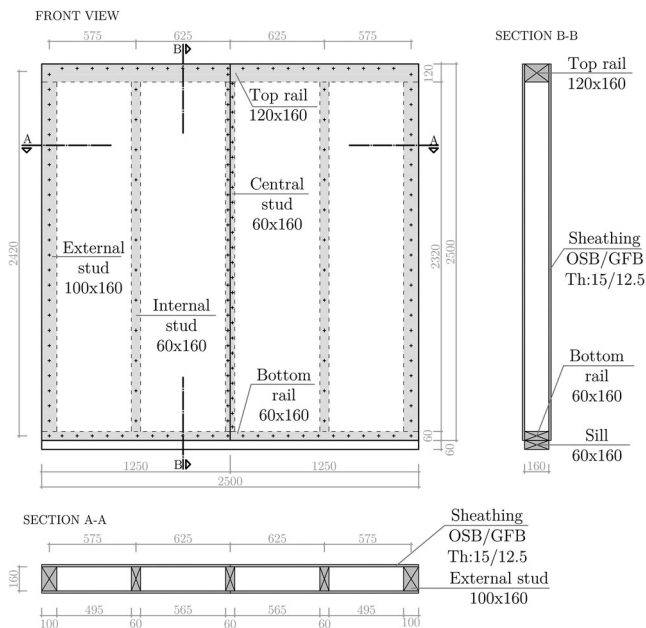


Figure 5. View of the partially anchored LTF shear wall tested by Grossi et al. (2015).

more different than the first-loading ones. The pinching paths of the RC portal have opposite concavity to those of the LTF shear wall.

In Figure 8(c,d), the dissipated energy is divided into fractions related to the first-loading and re-loading parts of the curves. The fractions of dissipation due to the re-loading curves are 82 and 84% in the RC and LTF,

respectively. The similarity of the 2% descends from the differences in the loading protocol. Therefore, the loading protocol effects could be partially removed from the analysis by estimating an average dissipated energy, i.e. the average dissipated energy per unit of displacement obtained by dividing the maximum energy value with the cumulative displacement associated with the particular path. Figure 8(a,b) shows the average dissipated energy per unit of displacement corresponding to the first-loading and re-loading curves.

The averaged dissipated energy corresponding to the force-displacement curves is 77% in the RC portal and 21% in the LTF shear wall. The concavity opposition determines a significant disproportion between the two systems' performance after damage. The RC base joints preserve significant dissipation capacity while the hold-downs run out of their potential after plasticisation. This crucial difference manifests in the opposition of the concavity of the force-displacement curves, see the qualitative illustration in Figure 1. The RC curvature has the same concavity of the first-loading, while LTF has concavity contrary to the first-loading curve. The backbone curves of the two systems appear similar. However, the RC structure retains an extra energy, marked in Figure 1, which causes additional dissipation in RC base joints.

Note that the experimental investigation refers to an LTF structure. Still, it is representative of all timber structures whose resistance depends on the interaction between the wood fibres and a metal fastener. In this article, the

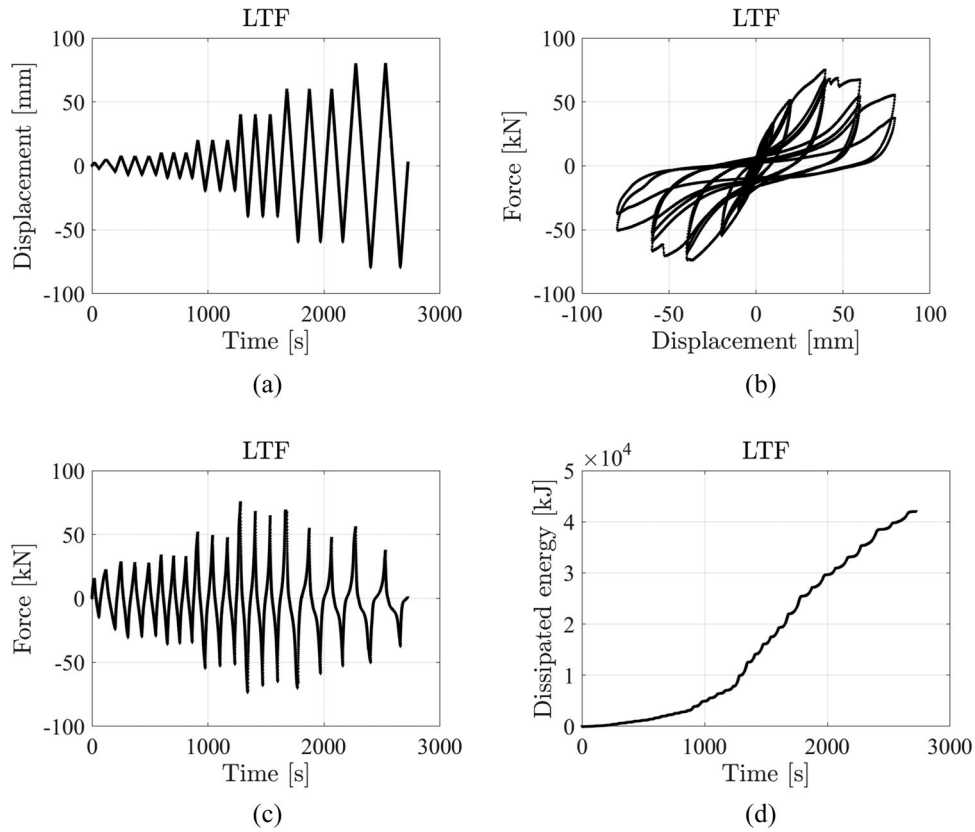


Figure 6. (a) Displacement protocol, (b) hysteresis loop, (c) force-time and (d) dissipated energy-time functions of the LTF frame under cyclic loading (Grossi et al., 2015).

Table 1. Synthetic comparison between the performance of the two systems in terms of resistance F_{\max} , yielding horizontal displacement d_y , ultimate horizontal displacement d_u and ductility $\mu = d_y/d_u$.

Parameter	RC	LTF	Difference (%)
F_{\max} (kN)	77.3	65.5	18.0
d_y (mm)	22.0	36.4	-39.6
d_u (mm)	60.0	53.5	12.1
$\mu = \frac{d_y}{d_u}$	2.7	1.5	85.6

mechanical reasons behind the opposing pinching effects are investigated. The research focuses on assessing the impact of these differences on seismic performance using the chosen experimental data.

5. Effect of diverse pinching on the seismic response

The seismic performance of the RC and LTF archetypes modelled as single-degree-of-freedom (SDOF) systems are paralleled. The resisting force is simulated by an empirical hysteresis model, while the mass is arbitrarily assumed equal to 21 ton. The value originates by multiplying the two archetypes' approximate resistance force (≈ 70 kN) with the earthquake's maximum intensity measure (IM), equal to 0.3 g. In the first part, the methods supporting the estimate of the fragility functions are introduced. In the second part, the nonlinear dynamic analyses' results and the fragility estimates of the two archetypes associated with the repetition of three earthquakes are illustrated and discussed.

5.1. Modelling and choice of the seismic hazard scenario

The following nonlinear ordinary differential equation describes the cyclic response of the RC and LTF archetypes modelled as SDOF systems. Multiple scholars use SDOF systems to isolate the consequences of a phenomenon (see Amadio et al., 2003). Adopting multi-degrees of freedom systems to reproduce the hysteretic response of a one-storey RC or LTF structural archetypes would be helpful when extending the validity of the results to different structural arrangements.

However, the consequences of pinching to two exemplary structural archetypes in terms of failure probability are explained. Failure probability derives from comparing the inter-storey drift demand with a given capacity value. The definition of the demand-capacity inequality in terms of inter-storey drift, a standard method in RC and LTF structures, supports an SDOF dynamic analysis of the considered archetypes, where the sole storey displacement is required for the failure estimate. This simplification does not undermine the reliability of the dynamic analysis since the empirical hysteresis model satisfactorily fits the experimental data.

The explicit fourth-order Runge-Kutta method is used for the temporal discretisation of the approximate solution of Equation (1).

$$m\ddot{x} + f_s = -m\ddot{x}_g \quad (1)$$

where m is the mass, x the displacement, \ddot{x} the double derivative of x with respect to time, f_s the resisting inelastic

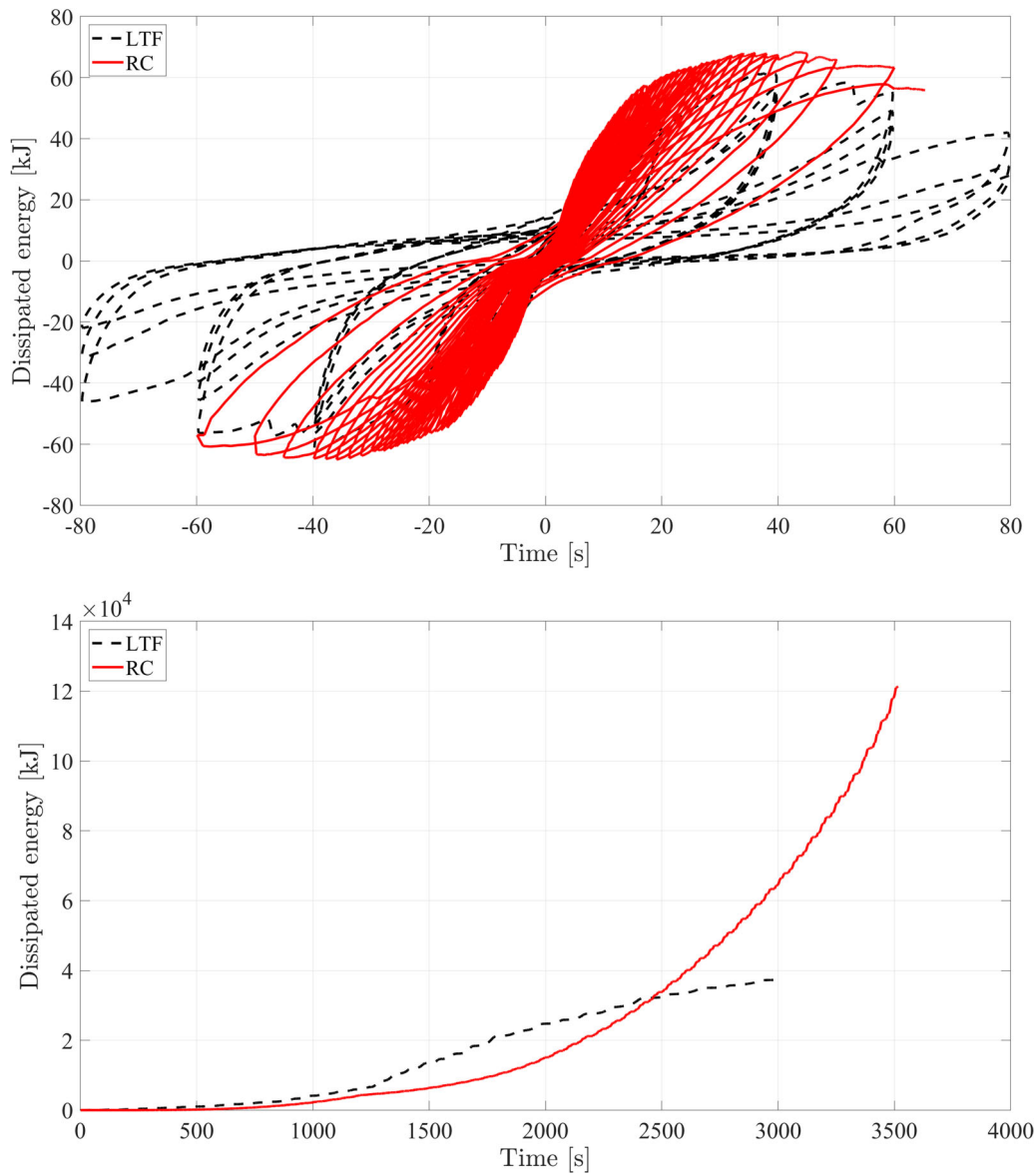


Figure 7. Comparison between the experimental cyclic response of the RC and LTF structures in terms of (a) force-displacement and (b) dissipated energy.

force, and \ddot{x}_g the ground acceleration. In this research, a modification of the Atan model, presented by Aloisio, Sejkot, Iqbal, and Fragiaco (2021), reproduces the resisting inelastic force. Sengupta and Li (2016) reviewed the hysteresis models for RC and timber structures, and reported a significant variety of modelling choices. A modification of the Atan model is chosen due to the computational and stability advantages.

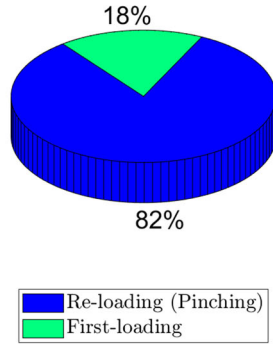
The Atan model replicates the hysteretic response of structural systems with pinching and degradation. In this modification, the arctangent function used for the re-loading and un-loading paths is replaced with a power function to achieve a more satisfactory correspondence. The Atan model uses the arctangent function in both the first-loading and re-loading curves. However, the arctangent function, distinguished by a certain curvature sign, cannot accurately reproduce pinching paths characterised by an opposite sign of their curvature. Therefore, they used a power function in place of the arctangent function in the re-loading paths to accurately mirror the experimental concavity of the

hysteresis loop with a different concavity of the re-loading paths. Specifically, exponents higher than one generate a power function characterised by the same concavity of LTF, while exponents lower than one can reproduce the concavity of the pinching paths of RC structures.

The Appendix reports the model's mathematical details and the estimated parameters obtained from a least-squares optimisation. The proposed model has been validated on the experimental cyclic response of existing test specimens from the scientific literature in Aloisio, Sejkot, et al. (2021). Figures 9 and 10 compare the experimental cyclic response with the outcomes of the empirical hysteresis model. The correspondence is quite accurate. Precisely, the RC re-loading paths have concavity opposite to that of the LTF (see Table A1).

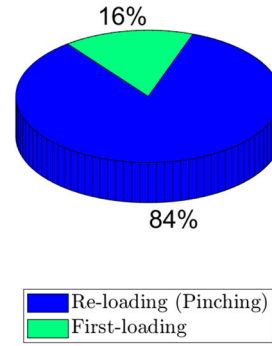
Figure 11 shows the displacement response of the RC and LTF systems under the repetition of three El Centro earthquakes. Interestingly, the maximum displacement of the RC does not exhibit significant differences between the three ground-motions, see Figure 12 and Table 2.

Dissipation in RC portal [kJ]



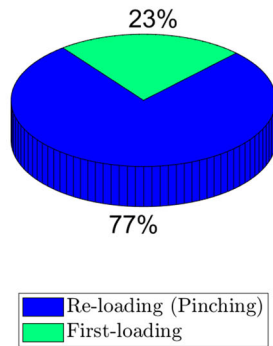
(a)

Dissipation in LTF shear wall [kJ]



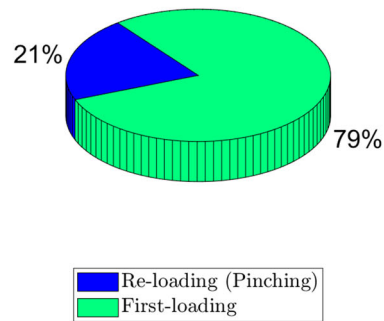
(b)

Dissipation in RC portal [kJ/mm]



(c)

Dissipation in LTF shear wall [kJ/mm]



(d)

Figure 8. Decomposition of the dissipated energy into two fractions related to the first loading and re-loading (pinched) paths; (a,b) are expressed in terms of total energy (kJ), while (c,d) in terms of the dissipated energy per unit of displacement.

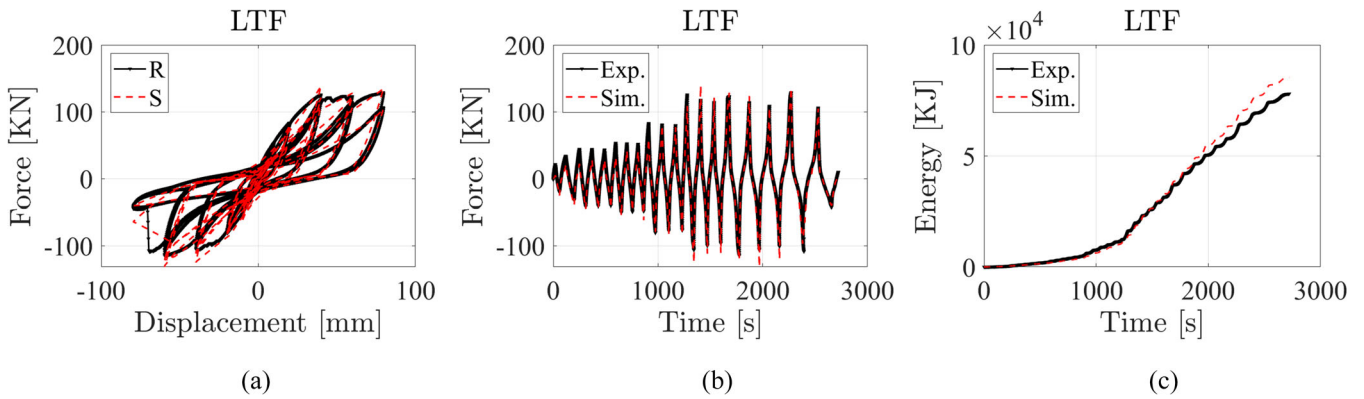


Figure 9. Superposition between the experimental cyclic response of the LTF specimen with that simulated by a modification of the Atan model.

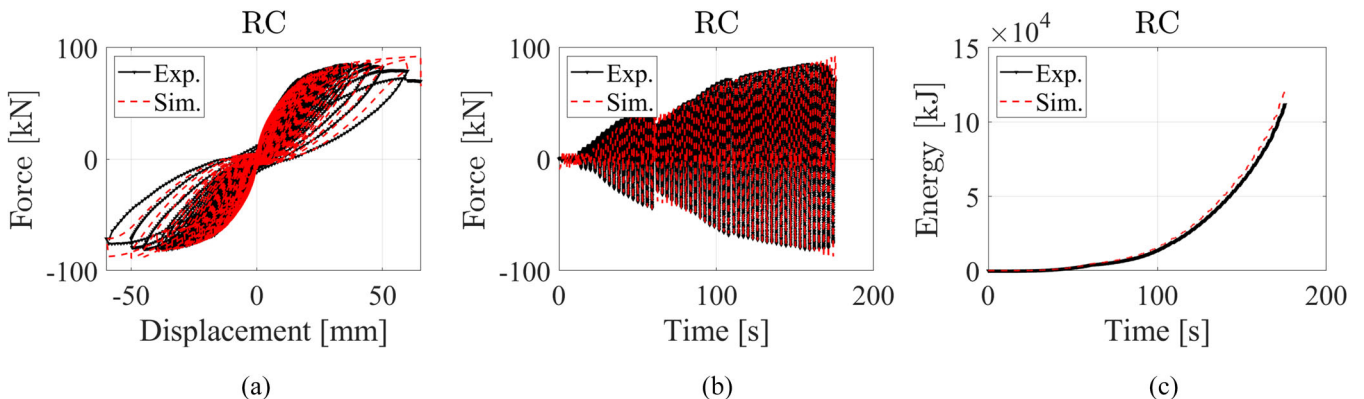


Figure 10. Superposition between the experimental cyclic response of the RC specimen with that simulated by a modification of the Atan model.

Conversely, the maximum displacement response of the LTF increases significantly from a direct inspection of Figure 12(c) and Table 3. The discrepancy between the two systems becomes far more manifest from Incremental Dynamic Analysis (IDA). Figure 12 shows the Truncated Incremental Dynamic Analysis (TIDA) of the two systems up to a 1.5 g PGA using the El Centro earthquake. While the maximum displacement of the RC portal after three earthquakes remains relatively stable, the maximum displacement of LTF increases dramatically during the second shock.

The inspection of Figure 11 reveals an unexpected phenomenon. The IDA curves referring to the first and third earthquakes sometimes overlap and interlace. Theoretically, this event should not happen, and the displacement demand associated with the third repetition should always be higher than the first one. Nevertheless, the progressive damage of the structure, leading to lowering natural frequencies, may be beneficial under particular seismic excitations. The earthquake might not have adequate frequency content in correspondence to the damaged structure's lowered natural frequencies. Consequently, the damage can be beneficial in a few occurrences, leading to a lower displacement demand.

The simple demonstration in Figure 11 encouraged a more systematic approach based on an extended set of ground motion earthquakes. Following the approach in Aloisio, Alaggio, and Fragiaco (2021), the list of 41 Italian earthquake records with magnitude ranging between

5 and 6.5, given in Table A2, represented the base for generating 41 artificial earthquakes, scaled to the same PGA and optimised to match the design spectrum in Figure 13. The 41 earthquakes correspond to all Italian earthquakes recorded since 1972 with $\text{PGA} \geq 0.4 \text{ g}$. The chosen PGA threshold became a reference for selecting the seismic scenario. The design spectrum, marked in red in Figure 13(a), corresponds to the seismic scenario expected in L'Aquila, Italy, according to the National Seismic Code.

The algorithm presented by Ferreira, Moutinho, Cunha, and Caetano (2020) yielded scaled the accelerograms for the TIDA, based on coherent inputs. The algorithm modifies the frequency content without producing substantial shape modifications. Figure 13(a) proves that the elastic response spectra in term of acceleration of the 41 earthquakes provide a valuable fit of the design spectrum. Therefore, the 41 earthquakes were enough to achieve a satisfactory fitting of the design response spectrum (Bojórquez & Iervolino, 2011). Additionally, Figure 13(b) depicts the elastic response spectra of the 41 earthquakes in terms of displacement.

The maximum displacement collected from each analysis, corresponding to a given earthquake and IM, is compared to the ultimate displacement of RC and LTF in Table 1 to assess the occurrence of failure. The authors chose the PGA rather than other IMs (Bojórquez, Iervolino, Reyes-Salazar, & Ruiz, 2012; Buratti, 2012; Jamshidiha, Yakhchalian, & Mohebi, 2018; Málaga-Chuquitaype & Bougatsas, 2017;

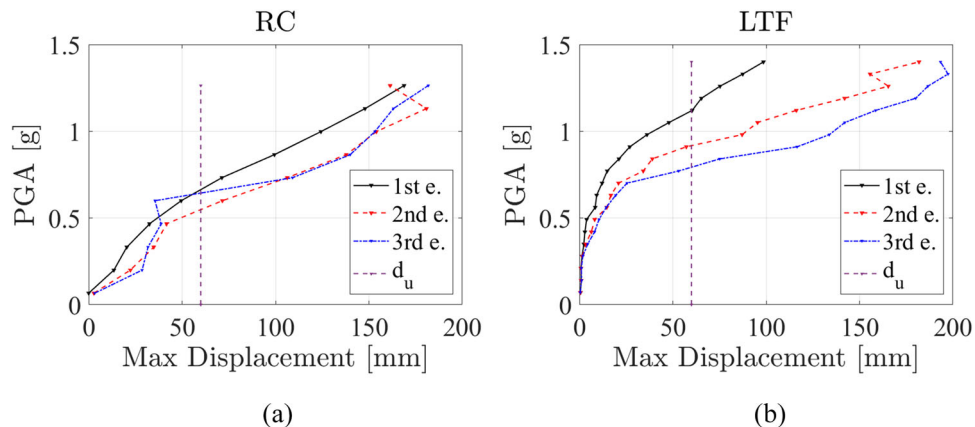


Figure 11. Truncated incremental dynamic analysis (IDA) of the RC and LTF archetypes up to 1.5 peak ground acceleration (PGA) of the El Centro earthquake.

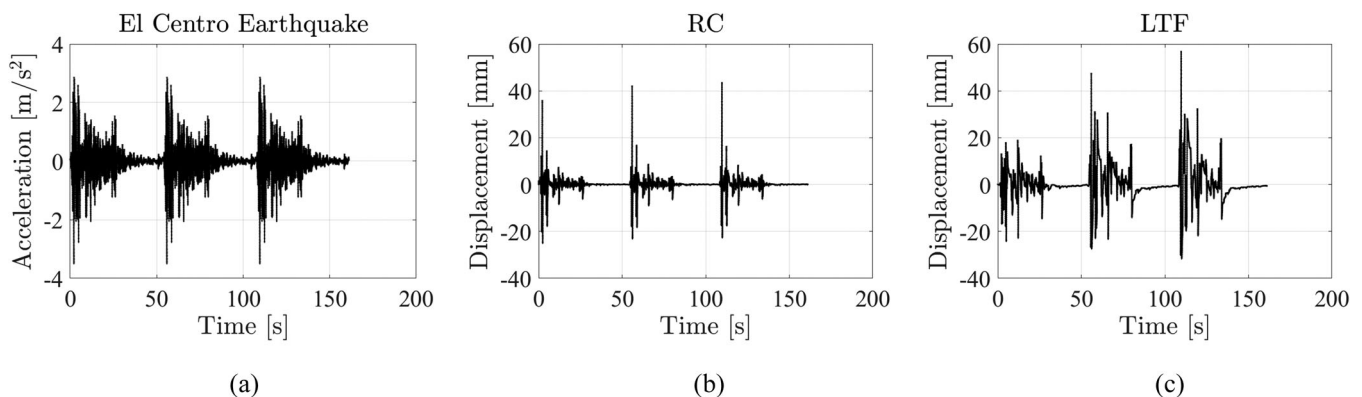


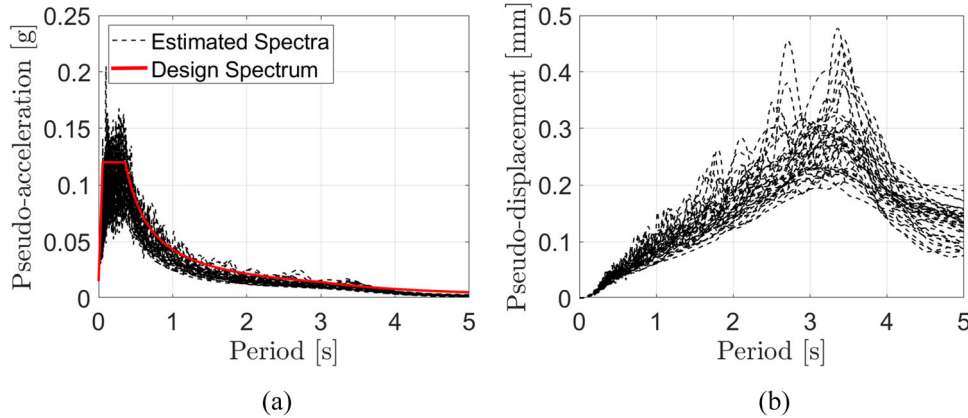
Figure 12. Seismic performance of the RC frame during the El Centro earthquake.

Table 2. Estimation of the seismic performance of the RC portal with a 20 ton top mass under the repetition of three El Centro earthquakes (e.).

Control parameters	First e.	Second e.	Third e.	First-second e. (%)	First-third e. (%)
Max drift (mm)	36	42	43	17	19
Dissipated energy (d.e.) (kJ)	11	11	21	0	98
d.e. first loading (%)	23	6	3	-74	-87
d.e. pinching (%)	77	94	97	22	26

Table 3. Estimation of the seismic performance of the LTF shear wall with a 20 ton top mass under the repetition of three El Centro earthquakes (e.).

Control parameters	First e.	Second e.	Third e.	First-second e. (%)	First-third e. (%)
Max drift (mm)	19	47	57	151	201
Dissipated energy (d.e.) (kJ)	11	14	24	32	127
d.e. first loading (%)	19	8	4	-58	-79
d.e. pinching (%)	81	92	96	14	19

**Figure 13.** Acceleration and displacement elastic spectra.

Minas & Galasso, 2019; Yakhchalian, Nicknam, & Amiri, 2015) because PGA is used to classify seismic hazards in Italy. The definition of the ultimate displacement is based on UNI EN 12512. If the maximum displacements surpass the values in Table 1, the archetypes reach collapse.

A lognormal cumulative distribution function (CDF) fits the fragility function from the failure probabilities associated with each IM (Baker, 2015):

$$P(F|IM = x) = \Phi \left[\frac{\ln(x/\theta)}{\beta} \right] \quad (2)$$

where $P(F|IM = x)$ is the probability that a ground motion with $IM = x$ will cause the structure to collapse; Φ is the standard normal CDF; θ is the median of the fragility function (the IM level with 50% probability of collapse); and β is the standard deviation of $\ln IM$. The parameters of the fragility functions, θ and β , originate from maximum likelihood estimation (Baker, 2015).

5.2. Results

Figure 14 shows the maximum displacement corresponding to each earthquake given a specific PGA. Each line identifies the response of the considered structural system to a given earthquake for increasing and discretised values of the PGA, in the range 0.1–0.6 PGA. The black, red and blue interpolating lines correspond to the structural response due to the first, second and third repetition of a given earthquake. The

horizontal dotted line identifies the ultimate displacement d_u in Table 1, assumed as collapse condition.

The plots of the TIDA results might be confusing. Still, the scatter between the two systems' responses under repeated cycles is more marked in LTF than RC. An immediate inspection of Figure 14 proves that the diverse pinching causes marked differences between the two archetypes, especially after repeated cycles. Accurately, the ductility and resistance primarily drive the seismic performance after a single earthquake. However, if successive earthquakes occur, the LTF reaches collapse with lower PGAs: the discrepancy between RC and LTF increases. The dissipation capacity of LTF is less stable than RC after multiple cycles due to the opposite concavity of the re-loading paths. Interestingly, resistance and ductility are not the sole parameters to characterise the structural response after multiple high-amplitude cycles.

The maximum displacements collected in Figure 14 are used to estimate the fragility of RC and LTF. Figure 15 shows the estimated cumulative lognormal distributions. The black curves distinguish the fragility of RC, while the red ones that of LTF. There are three curves per archetype associated with the fragility after the first, second and third earthquake. The performance of RC and LTF is more unmistakable than in Figure 14.

After the first earthquake, the fragility curves of RC and LTF are very alike, although the LTF seems to be less fragile than RC. Still, the fragility of LTF increases dramatically after the second shock, while that of RC remains very stable

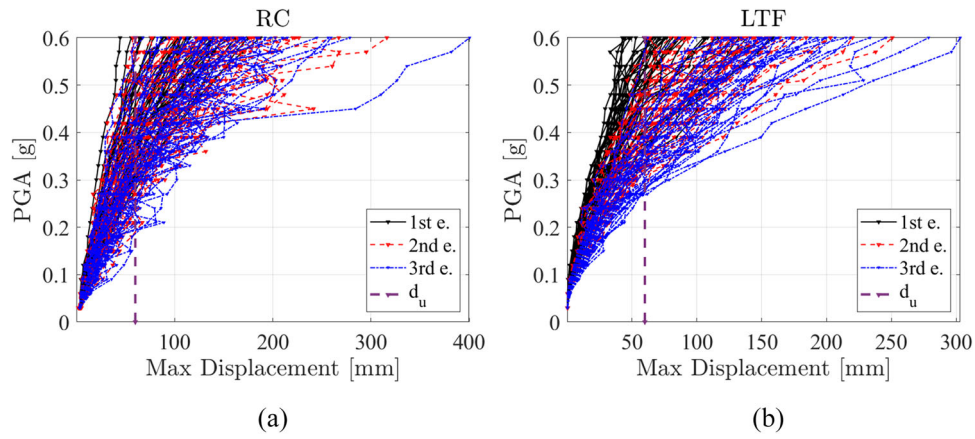


Figure 14. Truncated incremental dynamic analysis (TIDA) of the RC (a) and LTF (b) archetypes under the chosen earthquakes. The e. in the legend stands for earthquake, while d_u is the ultimate displacement according to Table 1.

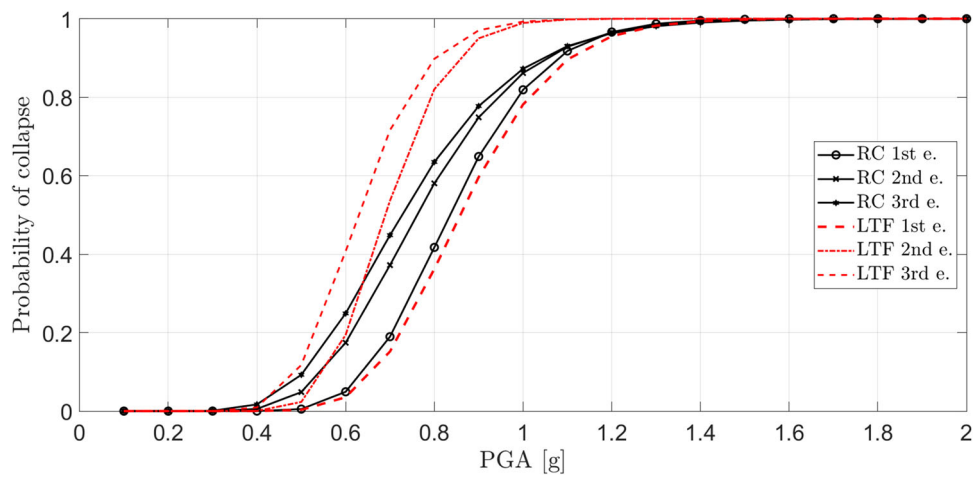


Figure 15. Fragility functions of the considered structural systems under repeated cycles, e. stand for earthquake.

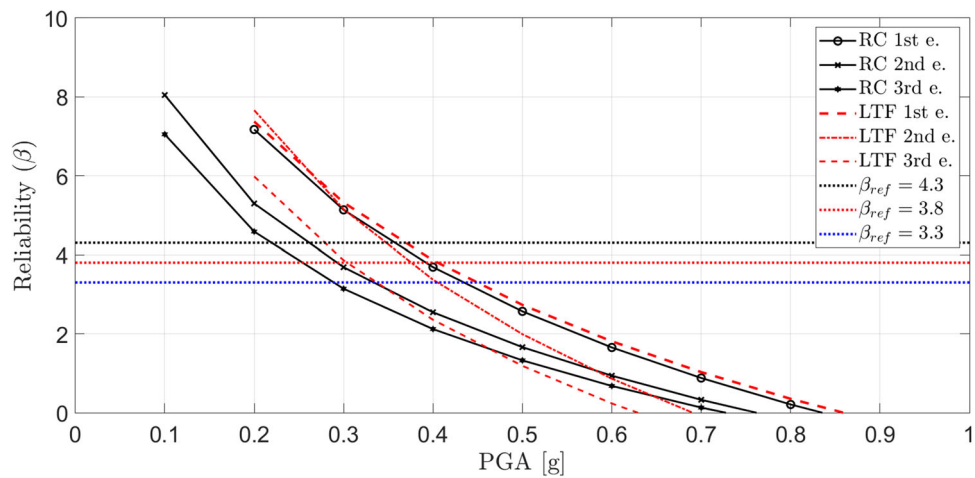


Figure 16. Reliability indexes of the considered structural systems under repeated cycles, e. stand for earthquake.

Table 4 Recommended minimum values of β_d and related failure probability P_f .

Reliability class	β_d	P_f
RC3	4.3	8.50E-06
RC2	3.8	7.20E-05
RC1	3.3	4.80E-04

compared to LTF. After the third earthquake, the fragility of RC and LTF increase further. In both systems, the difference between the response after the first and the second earthquake is more marked than that between the second and the third. Still, the discrepancy between the fragilities after the second and the third shocks is higher in LTF than in RC systems.

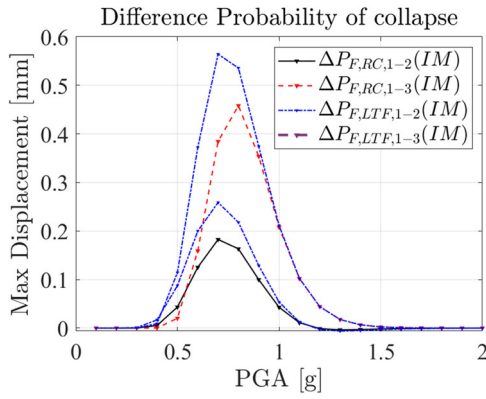


Figure 17. Differences between the failure probabilities due to repeated cycles. In the legend, Δ expresses the difference in the failure probabilities (P_F) of a given archetype (RC or LTF) between the first and second (Equations (1) and (2)) or first-third (Equations (1)–(3)) earthquakes.

The reliability indexes β are also used to assess the diverse seismic response of RC and LTF after repeated cycles (see Figure 16). The basic reliability targets for the ultimate limit state recommended in EN 1990 (2002) are based on a semi-probabilistic approach, with the target value of reliability index $\beta_d = 3.80$ for a 50 years reference period (see Table 4). The reliability targets can be correctly derived from the failure probability.

The value of reliability indicators depends on the related probabilistic approach. Many probabilistic methods have therefore been developed to carry out reliability analyses. In the recent past, many researchers have followed numerical procedures, such as Monte Carlo simulations. Other approximate and well-acknowledged methods are the first and second-order reliability methods (FORM and SORM). This article follows the classical definition of reliability after (Cornell, 1969). The Cornell reliability index (β_r) can be obtained from the failure probability $P(C|IM = x)$ by the following inversion (Cornell, 1969):

$$\beta_r = \Phi(1 - P(C|IM = x)) \quad (3)$$

However, in the chosen input conditions, the difference between RC and LTF is not evident for the reliability values in Table 4. If the reliability threshold is lower than 2 (see Figure 16), the same evidence found from the inspection of the fragility functions in Figure 15 arises: the seismic performance of LTF after repeated cycles increases notably.

The difference between the collapse probabilities in Figure 15 explains the discrepancy between RC and LTF further. Figure 17 plots the difference between first-second and second-third earthquakes fragility curves of the RC and LTF specimens. The difference between the RC and LTF specimens is pronounced if the PGA ranges between 0.5 and 1g. As further evidence of the diverse pinching effect, the discrepancies in failure probability associated with LTF are more than two times those of RC.

6. Discussion

The fragility function computed from the first earthquake response represents the fragility before the earthquake. It expresses the potential consequences of an earthquake

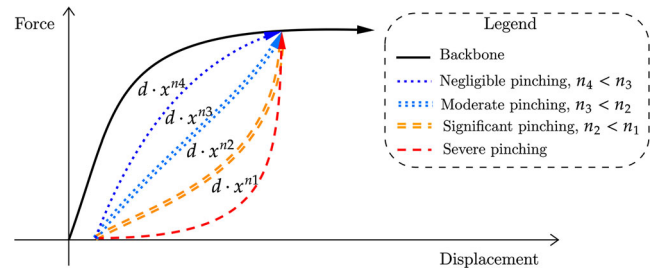


Figure 18. Qualitative illustration of the effect of variable pinching obtained by varying the exponent of the power function in Equation (6).

before its occurrence. Conversely, the fragility after the second shock represents the fragility after an earthquake. Fragility functions before and after an earthquake are strongly related to structural resilience (Dong & Frangopol, 2015).

Resilience is a comprehensive concept. In civil engineering, it is the system capacity to lessen the consequences of a shock, absorb the shock if it occurs, and recover quickly after it (Bruneau & Reinhorn, 2006; Cimellaro, Renschler, Reinhorn, & Arendt, 2016). A resilient system should have reduced failure probabilities, reduced consequences from failures and reduced recovery time. According to Bruneau and Reinhorn (2006), robustness, redundancy, resourcefulness and rapidity concur to structural resilience.

The considered RC and LTF specimens have a similar probability of collapse before the earthquake. However, they exhibit diverse robustness. Robustness expresses the capacity to withstand a given level of stress or demand without suffering degradation or loss of function. RC exhibits lower degradation compared to LTF, representative of timber structures *tout court*.

The following elementary measure of robustness is proposed:

$$I_{R,i} = \frac{P_{F,i}|\widehat{IM}}{P_{F,1}|\widehat{IM}} \quad (4)$$

$$\widehat{IM} = \arg \max_{IM} [P_{F,1}|IM - P_{F,i}|IM] \quad (5)$$

where $I_{R,i}$ is the index of robustness after the i th $|i| > 2$ earthquake, $P_{F,i}|\widehat{IM}$ is the failure probability after the i th earthquake given \widehat{IM} , $P_{F,1}$ is the failure probability after the first earthquake given \widehat{IM} . Table 4 reports the obtained $I_{R,i}$ values of the considered RC and LTF specimens. The $I_{R,i}$ indicator ranges from 0 to 1, where 1 expresses the optimum robustness in case of non-degrading system.

RC's robustness index after the first and second earthquake is 51 and 41%. These percentages reduce to 13 and 2% for LTF, highlighting the more severe consequences of structural degradation. Damage in the timber structure is mainly localised in the connections. Likely, the timber-connector dissipation potential cannot be restored unless additional connectors are installed in un-damaged locations. Subsequently, un-damaged wood fibres can withstand further damage. Conversely, the consequences of damage in an RC structure are lower than LTF.

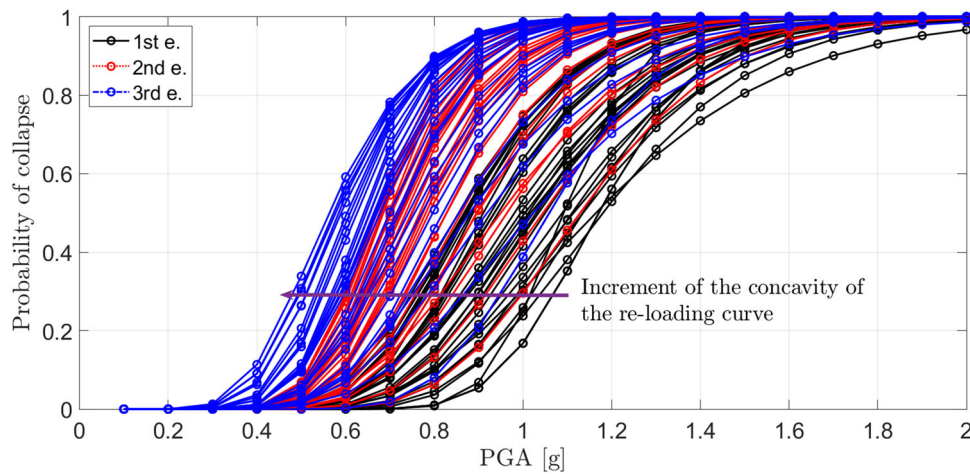


Figure 19. Fragility functions of the considered structural systems with variable pinching under repeated cycles, e. stand for earthquake. The arrow direction indicates the curves associated with a higher concavity of the pinching path.

The RC portal was designed according to the Italian seismic provisions, as evidenced by the reinforcement in the beam-to-column joint. Likely, adopting these measures reduces seismic fragility and has a beneficial impact on seismic resilience. Parallely, adequate resilience measures must be adopted in the design of timber structures. Conventional nailed or screwed connections are intrinsically non-resilient due to the extensive damage of timber. Accordingly, the adoption of friction-based connections embodies the leading frontier in timber engineering for enhancing structural resilience (Hashemi, Zarnani, Masoudnia, & Quenneville, 2018; Huang & Chang, 2017). However, the applications of these connections, also known as resilient connections, are still limited, despite the extended research investigations in the last decade.

The comparison between RC and LTF in terms of redundancy, resourcefulness and rapidity does not emerge directly from this article results. Therefore, a proper comparison in terms of structural resilience entails assessing the economic and social consequences of failure in both structures. However, all of them being equal, LTF is less resilient than RC due to lower robustness. This research quantified the diverse seismic performance of RC and timber archetypes. Diverse pinching leads to a notably different structural robustness, affecting the so-called structural resilience.

7. Effect of variable re-loading path concavity on structural robustness

Several scholars and the above investigations identify pinching as the primary weakness of timber structures (Di Gangi, Demartino, Quaranta, & Monti, 2020). Therefore, some researchers devised alternative strategies to reduce or eliminate pinching. Dissipation devices, added as coupling elements between timber shear walls, increase the dissipation capacity due to the sole connections, reducing the consequences of pinching (Kramer, Barbosa, & Sinha, 2016).

This solution does not eliminate pinching but enhances the structural dissipation sources. Other scholars attempted to eliminate pinching by developing pinching-free

connections (Chan, Hashemi, Zarnani, & Quenneville, 2021; Li et al., 2021). This solution improves the cyclic behaviour significantly, as demonstrated from multiple experimental tests (Loo, Quenneville, & Chouw, 2016): the mutual sliding between metal plates with interposed shim material guarantees an almost Coulomb-like dissipation.

Accurate modelling of the lateral response of timber structures entails a faithful simulation of the pinching paths with their exact curvature. This section investigates the effect of variable pinching of the LTF structural archetype in Figure 5. The considered structural systems, obtained by varying the power function exponent in the range of 0.1–3, are ideal structures, possibly obtained in reality by adopting pinching-free connectors, dissipating devices or different connections arrangements. In this section, the technical aspects related to seismic performance improvement are not addressed. However, experimental tests on timber structures showed that the re-loading curve's curvature could synthetically represent the effect of pinching. Figure 18 explains the effect of variable pinching, from negligible to severe effects. The curvature of the re-loading paths of the LTF specimen is modified, obtaining a range of fictitious structural systems characterised by identical backbone curves but different dissipated energy after the repetition of multiple cycles. They carried out nonlinear dynamic analyses of the chosen structural archetypes under three repetitions of the 41 selected earthquakes, as described in the previous paragraphs.

Figure 19 depicts the fragility functions of the fictitious structural systems, derived from the LTF one in Figure 5 by varying the exponent of the power function representative of the pinching path concavity. As anticipated, the structural fragility rises as the number of earthquake repetition and the pinching effect increase. This effect manifests in the leftwards shift of the fragility functions. Still, the estimate of the outgrowths of pinching is challenging from the direct inspection of the fragilities. Hence, the robustness index, defined in Figure 4, provides a synthetic indication of the consequences of pinching under repeated cycles. The definition of the robustness index originates from the difference between the fragility functions, in Figure 20, corresponding to the same system, under earthquake repetitions. Therefore,

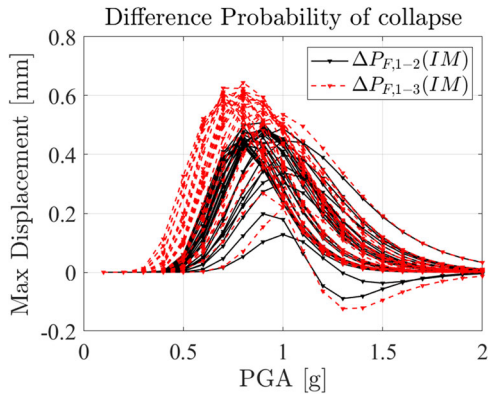


Figure 20. Differences between the failure probabilities due to repeated cycles of the structural systems with variable pinching. In the legend, Δ expresses the difference in the failure probabilities (P_f) of a given archetype (RC or LTF) between the first and second (Equations (1) and (2)) or first–third (Equations (1)–(3)) earthquakes as a function of the intensity measure (IM).

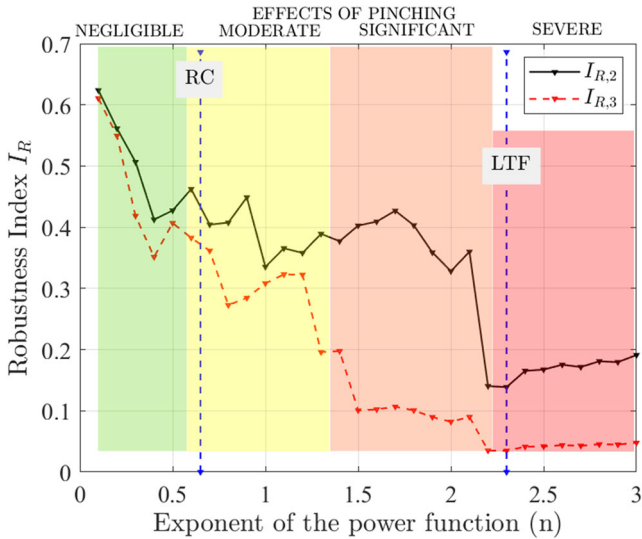


Figure 21. Robustness index of the considered structural systems with variable pinching. The pinching concavity is expressed by the exponent of the power function used to mirror the re-loading curves in Equation (6).

two robustness indexes are estimated, named $I_{R,2}$ and $I_{R,3}$, corresponding to the consequences after the second and third repetition, as formulated in Equation (4).

Figure 21 shows the variation of the two robustness indexes as a function of the concavity of the pinching path. Two vertical lines indicate the exponents of the power function used to represent the concavity of pinching curves in the RC and LTF structures, equal to 0.65 and 2.30, respectively. The effect of earthquake repetition determines a dramatic growth of the failure probability and a significant reduction of the robustness index.

The indexes corresponding to LTF are 0.13 and 0.02, shown in Table 5 as a result of the previous analyses. The indexes corresponding to the RC pinching ($n_1 = 0.65$) are lower compared to the ones in Table 5. The considered RC structure exhibits a higher ductility than LTF, leading to higher robustness indexes ($I_{R,2} = 0.51$ and $I_{R,3} = 0.42$), compared to the ones obtained from a hysteresis model distinguished by the same backbone of LTF, but the RC

Table 5. Robustness of RC and LTF archetypes under repeated cycles.

Robustness index $I_{R,i}$ [%]		
Earthquake	RC	LTF
First–second earthquake	0.51	0.13
First–third earthquake	0.42	0.02

pinching concavity ($I_{R,2} = 0.44$ and $I_{R,3} = 0.38$). Still, the minor differences evidence the preeminent role of pinching in affecting the seismic performance after multiple cycles.

The evolution of the robustness indexes enabled defining four qualitative regions of behaviour analogously to the qualitative ranking typical of fragility functions. The inspection of Figure 21 may suggest the partition of the concavity in terms of negligible, moderate, significant and severe pinching effects. The RC structure falls in the moderate pinching, while the LTF in the severe region. The partition is qualitative and does not have an absolute meaning. Nevertheless, it has an illustrative purpose and expresses the potentiality of the presented robustness index for a structural performance classification inclusive of the effects of repeated cycles.

The integration between the robustness index and the estimate of the social, economic and environmental consequences of repeated cycles would lead to a synthetic measure of structural resilience. The presented robustness index embodies the structural aspect of resilience. Figure 21 reveals that a modest improvement of the pinching response of timber structures, using dissipating devices or non-conventional pinching-free connections, can lead to a remarkable increment of the structural performance.

8. Conclusions

Pinching characterises the hysteretic response of several structural systems. Pinching is the act of penetration between a pinching and a pinched element. The possible effect of local damage due to the act of pinching manifests in a reduced stiffness after the first load cycle. The article discusses the effect of diverse pinching in RC and LTF structures. The RC portal's re-loading paths have opposite concavity to those of the LTF shear wall. The concavity opposition determines a lower dissipation capacity of LTF than RC under multiple cycles, although the RC and LTF specimens have similar resistance and ductility. The average fraction of the dissipated energy due to pinching is 77% in RC and 21% in LTF. Thus, the concavity opposition determines a significant disproportion between the two systems' performance after damage.

The TIDA of the two systems modelled as SDOF oscillators yielded the fragility curves, approximated by a lognormal CDF. The failure probability of LTF increases dramatically after the second and third repetition of the same earthquake, while that of RC remains quite stable. The stability of RC under repeated cycles reveals its significant resilience compared to LTF structures. The current analysis proved that ductility and resistance primarily drive the seismic response after a single earthquake. However, the performance after multiple earthquakes strongly depends on

the pinching phenomenon, generally neglected in standard design practices. The article discusses a robustness index $I_{R,i}$, ranging from 0 to 1, which quantifies the capacity to withstand a given level of stress without suffering degradation. A non-degrading system is associated with $I_{R,i} = 1$. For example, the robustness index of RC reaches 0.42 after two earthquakes, that of LTF reduces to 2% under the same inputs.

Nonlinear dynamic analyses are carried out to characterise the response of the LTF archetype by assuming a variable concavity of the re-loading curve. The analyses led to the estimate of the robustness indexes as a function of the pinching concavity, highlighting four regions of behaviour associated with negligible, moderate, significant and severe pinching. The comparison between constructive technologies will be further investigated by developing more realistic case studies representative of the two systems. Additionally, they will attempt to estimate the economic, environmental and social consequences of pinching for a direct quantification of structural resilience.

Disclosure statement

No potential conflict of interest was reported by the author(s).

Data availability statement

All data, models or code that support the findings of this study are available from the corresponding author upon reasonable request.

ORCID

Angelo Aloisio  <http://orcid.org/0000-0002-6190-0139>

References

- Abdollahzadeh, G., Mohammadgholipour, A., & Omranian, E. (2019). Seismic evaluation of steel moment frames under mainshock–after-shock sequence designed by elastic design and PBPD methods. *Journal of Earthquake Engineering*, 23(10), 1605–1628. doi:10.1080/13632469.2017.1387198
- Abdollahzadeh, G., & Sadeghi, A. (2018). Earthquake recurrence effect on the response reduction factor of steel moment frame. *Asian Journal of Civil Engineering*, 19(8), 993–1008. doi:10.1007/s42107-018-0079-3
- Aloisio, A., Alaggio, R., & Fragiaco, M. (2021). Equivalent viscous damping of cross-laminated timber structural archetypes. *Journal of Structural Engineering*, 147(4), 04021012. doi:10.1061/(ASCE)ST.1943-541X.0002947
- Aloisio, A., Alaggio, R., Köhler, J., & Fragiaco, M. (2020). Extension of generalized bouc-wen hysteresis modeling of wood joints and structural systems. *Journal of Engineering Mechanics*, 146(3), 04020001. doi:10.1061/(ASCE)EM.1943-7889.0001722
- Aloisio, A., Boggian, F., Roberto, T., & Fragiaco, M. (2021). The role of the hold-down in the capacity model of clt andltf shear walls based on the experimental lateral response. *Construction and Building Materials*, 289, 123046. doi:10.1016/j.conbuildmat.2021.123046
- Aloisio, A., Sejkot, P., Iqbal, A., & Fragiaco, M. (2021). An empirical transcendental hysteresis model for structural systems with pinching and degradation. *Earthquakes Engineering and Structural Dynamics*, 50, 2277–2293. doi:10.1002/eqe.3442
- Amadio, C., Fragiaco, M., & Rajgelj, S. (2003). The effects of repeated earthquake ground motions on the non-linear response of SDOF systems. *Earthquake Engineering & Structural Dynamics*, 32(2), 291–308. doi:10.1002/eqe.225
- Baber, T. T., & Noori, M. N. (1985). Random vibration of degrading, pinching systems. *Journal of Engineering Mechanics*, 111(8), 1010–1026. doi:10.1061/(ASCE)0733-9399(1985)111:8(1010)
- Baker, J. W. (2015). Efficient analytical fragility function fitting using dynamic structural analysis. *Earthquake Spectra*, 31(1), 579–599. doi:10.1193/021113EQS025M
- Bergami, A. V., & Nuti, C. (2015). Experimental tests and global modeling of masonry infilled frames. *Earthquakes and Structures*, 9(2), 281–303. doi:10.12989/eas.2015.9.2.281
- Bojórquez, E., Baca, V., Bojórquez, J., Reyes-Salazar, A., Chávez, R., & Barraza, M. (2017). A simplified procedure to estimate peak drift demands for mid-rise steel and r/c frames under narrow-band motions in terms of the spectral-shape-based intensity measure inp . *Engineering Structures*, 150, 334–345. doi:10.1016/j.engstruct.2017.07.046
- Bojórquez, E., & Iervolino, I. (2011). Spectral shape proxies and non-linear structural response. *Soil Dynamics and Earthquake Engineering*, 31(7), 996–1008. doi:10.1016/j.soildyn.2011.03.006
- Bojórquez, E., Iervolino, I., Reyes-Salazar, A., & Ruiz, S. E. (2012). Comparing vector-valued intensity measures for fragility analysis of steel frames in the case of narrow-band ground motions. *Engineering Structures*, 45, 472–480. doi:10.1016/j.engstruct.2012.07.002
- Bruneau, M., & Reinhorn, A. (2006). Overview of the resilience concept. *Proceedings of the 8th US national conference on earthquake engineering* (Vol. 2040, pp. 18–22). Oakland, CA: Earthquake Engineering Research Institute.
- Buratti, N. (2012). A comparison of the performances of various ground–motion intensity measures. *Proceedings of the 15th world conference on earthquake engineering, Lisbon, Portugal* (pp. 24–28). Lisboa, Portugal: Sociedade Portuguesa de Engenharia Sismica (SPES).
- Casolo, S. (2017). A numerical study on the cumulative out-of-plane damage to church masonry façades due to a sequence of strong ground motions. *Earthquake Engineering & Structural Dynamics*, 46(15), 2717–2737. doi:10.1002/eqe.2927
- Chan, N., Hashemi, A., Zarnani, P., & Quenneville, P. (2021). Pinching-free connector for timber structures. *Journal of Structural Engineering*, 147(5), 04021036. doi:10.1061/(ASCE)ST.1943-541X.0002982
- Cimellaro, G. P., Renschler, C., Reinhorn, A. M., & Arendt, L. (2016). Peoples: A framework for evaluating resilience. *Journal of Structural Engineering*, 142(10), 04016063. doi:10.1061/(ASCE)ST.1943-541X.0001514
- Cornell, C. A. (1969). A probability-based structural code. *Journal Proceedings*, 66, 974–985. doi:10.5772/65894
- Di Gangi, G., Demartino, C., Quaranta, G., & Monti, G. (2020). Dissipation in sheathing-to-framing connections of light-frame timber shear walls under seismic loads. *Engineering Structures*, 208(110246), 110246. doi:10.1016/j.engstruct.2020.110246
- Dong, Y., & Frangopol, D. M. (2015). Risk and resilience assessment of bridges under mainshock and aftershocks incorporating uncertainties. *Engineering Structures*, 83, 198–208. doi:10.1016/j.engstruct.2014.10.050
- Elnashai, A., Bommer, J., & Martinez-Pereira, A. (1998). Engineering implications of strong-motion records from recent earthquakes. *Proceedings of 11th European conference on earthquake engineering*. Paris: European Association for Earthquake Engineering.
- Faisal, A., Majid, T. A., & Hatzigeorgiou, G. D. (2013). Investigation of story ductility demands of inelastic concrete frames subjected to repeated earthquakes. *Soil Dynamics and Earthquake Engineering*, 44, 42–53. doi:10.1016/j.soildyn.2012.08.012

- Favvata, M. J., & Karayannis, C. G. (2014). Influence of pinching effect of exterior joints on the seismic behavior of RC frames. *Earthquakes and Structures*, 6(1), 89–110. doi:10.12989/eas.2014.6.1.089
- Ferreira, F., Moutinho, C., Cunha, Á., & Caetano, E. (2020). An artificial accelerogram generator code written in Matlab. *Engineering Reports*, 2(3), e12129. doi:10.1002/eng2.12129
- Foliente, G. C. (1995). Hysteresis modeling of wood joints and structural systems. *Journal of Structural Engineering*, 121(6), 1013–1022. doi:10.1061/(ASCE)0733-9445(1995)121:6(1013)
- Folz, B., & Filiatrault, A. (2001). Cyclic analysis of wood shear walls. *Journal of Structural Engineering*, 127(4), 433–441. doi:10.1061/(ASCE)0733-9445(2001)127:4(433)
- Fragiacomo, M., Amadio, C., & Macorini, L. (2004). Seismic response of steel frames under repeated earthquake ground motions. *Engineering Structures*, 26(13), 2021–2035. doi:10.1016/j.engstruct.2004.08.005
- Grossi, P., Sartori, T., & Tomasi, R. (2015). Tests on timber frame walls under in-plane forces: Part 2. *Proceedings of the Institution of Civil Engineers - Structures and Buildings*, 168(11), 840–852. doi:10.1680/stbu.13.00108
- Guñez, F., Santa María, H., & Almazán, J. L. (2019). Monotonic and cyclic behaviour of wood frame shear walls for mid-height timber buildings. *Engineering Structures*, 189, 100–110. doi:10.1016/j.engstruct.2019.03.043
- Hashemi, A., Zarnani, P., Masoudnia, R., & Quenneville, P. (2018). Experimental testing of rocking cross-laminated timber walls with resilient slip friction joints. *Journal of Structural Engineering*, 144(1), 04017180. doi:10.1061/(ASCE)ST.1943-541X.0001931
- Hatzigeorgiou, G. D., & Beskos, D. E. (2009). Inelastic displacement ratios for SDOF structures subjected to repeated earthquakes. *Engineering Structures*, 31(11), 2744–2755. doi:10.1016/j.engstruct.2009.07.002
- Hosseinpour, F., & Abdelnaby, A. (2017). Fragility curves for RC frames under multiple earthquakes. *Soil Dynamics and Earthquake Engineering*, 98, 222–234. doi:10.1016/j.soildyn.2017.04.013
- Huang, H., & Chang, W.-S. (2017). Seismic resilience timber connection—adoption of shape memory alloy tubes as dowels. *Structural Control and Health Monitoring*, 24(10), e1980. doi:10.1002/stc.1980
- Jamrani, H. H., Amiri, J. V., & Rajabnejad, H. (2018). Energy distribution in RC shear wall-frame structures subject to repeated earthquakes. *Soil Dynamics and Earthquake Engineering*, 107, 116–128. doi:10.1016/j.soildyn.2018.01.010
- Jamshidiha, H., Yakhchalian, M., & Mohebi, B. (2018). Advanced scalar intensity measures for collapse capacity prediction of steel moment resisting frames with fluid viscous dampers. *Soil Dynamics and Earthquake Engineering*, 109, 102–118. doi:10.1016/j.soildyn.2018.01.009
- Jorissen, A., & Fragiaco, M. (2011). General notes on ductility in timber structures. *Engineering Structures*, 33(11), 2987–2997. doi:10.1016/j.engstruct.2011.07.024
- Kostinakis, K., & Athanatopoulou, A. (2016). Incremental dynamic analysis applied to assessment of structure-specific earthquake ims in 3d r/c buildings. *Engineering Structures*, 125, 300–312. doi:10.1016/j.engstruct.2016.07.007
- Kramer, A., Barbosa, A. R., & Sinha, A. (2016). Performance of steel energy dissipators connected to cross-laminated timber wall panels subjected to tension and cyclic loading. *Journal of Structural Engineering*, 142(4), E4015013. doi:10.1061/(ASCE)ST.1943-541X.0001410
- Li, Z., Chen, F., He, M., Zhou, R., Cui, Y., Sun, Y., & He, G. (2021). Lateral performance of self-centering steel-timber hybrid shear walls with slip-friction dampers: Experimental investigation and numerical simulation. *Journal of Structural Engineering*, 147(1), 04020291. doi:10.1061/(ASCE)ST.1943-541X.0002850
- Loo, W. Y., Quenneville, P., & Chouw, N. (2016). Rocking timber structure with slip-friction connectors conceptualized as a plastically deformable hinge within a multistorey shear wall. *Journal of Structural Engineering*, 142(4), E4015010. doi:10.1061/(ASCE)ST.1943-541X.0001387
- Luo, Q., He, M., Chen, F., & Li, Z. (2021). Probabilistic seismic performance assessment of timber-steel hybrid structures subjected to mainshock-aftershock sequences. *Soil Dynamics and Earthquake Engineering*, 141, 106532. doi:10.1016/j.soildyn.2020.106532
- Málaga-Chuquitaype, C., & Bougatsas, K. (2017). Vector-im-based assessment of alternative framing systems under bi-directional ground-motion. *Engineering Structures*, 132, 188–204. doi:10.1016/j.engstruct.2016.11.021
- Mansour, M., & Hsu, T. T. (2005). Behavior of reinforced concrete elements under cyclic shear. ii: Theoretical model. *Journal of Structural Engineering*, 131(1), 54–65. doi:10.1061/(ASCE)0733-9445(2005)131:1(54)
- Minas, S., & Galasso, C. (2019). Accounting for spectral shape in simplified fragility analysis of case-study reinforced concrete frames. *Soil Dynamics and Earthquake Engineering*, 119, 91–103. doi:10.1016/j.soildyn.2018.12.025
- Mitra, N. (2007). *An analytical study of reinforced concrete beam-column joint behavior under seismic loading* (Vol. 68). University of Washington, United States.
- Modica, A., & Stafford, P. J. (2014). Vector fragility surfaces for reinforced concrete frames in europe. *Bulletin of Earthquake Engineering*, 12(4), 1725–1753. doi:10.1007/s10518-013-9571-z
- Mouyiannou, A., Penna, A., Rota, M., Graziotti, F., & Magenes, G. (2014). Implications of cumulated seismic damage on the seismic performance of unreinforced masonry buildings. *Bulletin of the New Zealand Society for Earthquake Engineering*, 47(2), 157–170. doi:10.5459/bnzsee.47.2.157-170
- Ozcebe, G., & Saatcioglu, M. (1989). Hysteretic shear model for reinforced concrete members. *Journal of Structural Engineering*, 115(1), 132–148. doi:10.1061/(ASCE)0733-9445(1989)115:1(132)
- Park, R., Kent, D. C., & Sampson, R. A. (1972). Reinforced concrete members with cyclic loading. *Journal of the Structural Division*, 98(7), 1341–1360. doi:10.1061/JSDIAG.0003267
- Porcu, M. C. (2017). Ductile behavior of timber structures under strong dynamic loads. *Wood in Civil Engineering*, 2017, 173–196.
- Qin, X., & Chouw, N. (2017). Shake table study on the effect of mainshock-aftershock sequences on structures with sfsi. *Shock and Vibration*, 2017, 1–12. doi:10.1155/2017/9850915
- Raghunandan, M., & Liel, A. B. (2013). Effect of ground motion duration on earthquake-induced structural collapse. *Structural Safety*, 41, 119–133. doi:10.1016/j.strusafe.2012.12.002
- Salami, M. R., Kashani, M. M., & Goda, K. (2019). Influence of advanced structural modeling technique, mainshock-aftershock sequences, and ground-motion types on seismic fragility of low-rise RC structures. *Soil Dynamics and Earthquake Engineering*, 117, 263–279. doi:10.1016/j.soildyn.2018.10.036
- Sengupta, P., & Li, B. (2016). Hysteresis modeling of reinforced concrete structures: State of the art. *ACI Structural Journal*, 114(1), 25–38. doi:10.14359/51689422
- Wan, S., Loh, C. H., & Peng, S. Y. (2001). Experimental and theoretical study on softening and pinching effects of bridge column. *Soil Dynamics and Earthquake Engineering*, 21(1), 75–81. doi:10.1016/S0267-7261(00)00073-7
- Yakhchalian, M., Nicknam, A., & Amiri, G. G. (2015). Optimal vector-valued intensity measure for seismic collapse assessment of structures. *Earthquake Engineering and Engineering Vibration*, 14(1), 37–54. doi:10.1007/s11803-015-0005-6
- Zhai, C. H., Wen, W. P., Li, S., Chen, Z., Chang, Z., & Xie, L. L. (2014). The damage investigation of inelastic SDOF structure under the mainshock-aftershock sequence-type ground motions. *Soil Dynamics and Earthquake Engineering*, 59, 30–41. doi:10.1016/j.soildyn.2014.01.003

Appendix

A1. Hysteresis model

The hysteresis model descends from the formulation discussed by Aloisio, Sejkot, et al. (2021) based on the arctangent function. The model has the following piece-wise definition:

$$\begin{aligned}
1- & \arctan(bx - |c|) & \text{if } \{\dot{x} > 0, x > 0, x > \max[x(t)] \forall t \in [0, t]\} \\
2- & \arctan(bx + |c|) & \text{if } \{\dot{x} > 0, x < 0, x < \min[x(t)] \forall t \in [0, t]\} \\
3- & q \cdot d_1 x^{n_1} + f_r & \text{if } \{\dot{x} > 0, x > 0, x \leq \max[x(t)] \forall t \in [0, t]\} \\
4- & q \cdot d_2 x^{n_1} - f_r & \text{if } \{\dot{x} > 0, x < 0, x \geq \min[x(t)] \forall t \in [0, t]\} \\
5- & e_1 x^{n_2} - f_r & \text{if } \{\dot{x} < 0, x > 0\} \\
6- & -e_2 x^{n_2} + f_r & \text{if } \{\dot{x} < 0, x < 0\}
\end{aligned} \tag{A1}$$

Table A1. Parameters of the modified Atan model.

Parameter	RC	LTF
a	63.69	82.80
b	0.13	0.12
c	0.15	0.35
q	1.00	0.80
n_1	0.65	2.10
n_2	2.30	4.24

where the six conditional statements identify the transition between the different parts of the hysteresis. A set of three parameters define the arctangent function in each section of the loop: a characterise the amplitude of the force, b the x axis resolution and c the residual displacement. The additional parameters have the following definition based on the fulfilment of the continuity conditions between the branches of the loop. $d_1 = \{\max[F(t)] - f_r\} / \{\max[x(t)]^{n_1}\}$, $d_2 = \{\min[F(t)] + f_r\} / \{\min[x(t)]^{n_1}\}$, $e_1 = \{\max[F(t)]\} / \{\max[x(t)]^{n_2}\}$, $e_2 = \{\min[F(t)]\} / \{\min[x(t)]^{n_2}\}$, $f_r = \arctan(|c|)$. The exponents of the re-loading and un-loading branches depend on the peculiarities of the hysteresis curve. Table A1 resumes the values adopted in the current research. The chosen parameters descend from a least-squares optimisation.

Figure 7 presents the comparison between experimental and simulated data using the parameters in Table A1.

A2. List of earthquakes

The list of 41 Italian earthquake records with magnitude ranging between 5 and 6.5 is given in Table A2.

Table A2. List of earthquake recordings sorted from largest to smallest peak ground acceleration (PGA).

No	Year	Location (Italy)	Epical distance (km)	PGA (g)	Depth (km)	ML	MW
1	2016	Norcia	11.0	0.931	9.2	6.1	6.5
2	2016	Accumoli	8.5	0.851	8.1	6.0	6.0
3	2009	Fossa	3.6	0.652	17.1	5.4	5.5
4	2009	L'Aquila	4.9	0.644	8.3	5.9	6.1
5	2016	Visso	7.1	0.638	7.5	5.9	5.9
6	1976	Lusevra	6.2	0.632	6.8	6.1	5.9
7	2009	Monte Reale	7.9	0.550	9.4	5.3	5.4
8	2012	Medolla	9.3	0.495	8.1	5.8	6.0
9	1976	Lusevra	27.7	0.346	5.7	6.4	6.4
10	1976	Gemona del Friuli	16.2	0.342	11.3	6.0	6.0
11	1976	Friuli Venezia Giulia	9.4	0.322	4.3	5.8	5.6
12	1980	Laviano	33.3	0.314	15.0	6.5	6.9
13	2016	Castel Sant'Angelo sul Nera	9.4	0.295	8.1	5.4	5.4
14	2009	L'Aquila	11.0	0.294	11.0	5.1	5.4
15	2017	Cagnano amiterno	10.8	0.289	9.5	5.1	5.0
16	2009	L'Aquila	7.4	0.264	9.0	5.0	5.0
17	2012	Finale Emilia	16.1	0.259	9.5	5.9	6.1
18	2012	San Possidonio	6.9	0.252	7.2	5.1	5.5
19	1976	Nimis	7.0	0.241	13.3	5.5	5.1
20	1977	Trasaghis	7.1	0.238	10.8	5.3	5.3
21	2013	Fivizzano	11.9	0.227	7.0	5.2	5.1
22	2012	San Felice sul Panaro	7.4	0.205	5.0	5.1	9.1
23	1984	Perugia	20.6	0.201	6.0	5.2	5.6
24	2016	Norcia	4.4	0.191	8.0	5.4	5.3
25	1997	Foligno	20.1	0.184	5.5	5.4	5.4
26	1997	Foligno	21.6	0.184	5.7	5.8	6.0
27	2001	Naturno	25.9	0.167		5.3	4.8
28	1984	Villetta Barrea	17.4	0.158	12.1	5.7	5.5
29	1997	Foligno	24.2	0.152	5.7	5.6	5.7
30	2009	Pizzoli	10.1	0.148	9.7	5.0	5.1
31	1984	Settefrati	10.1	0.110	20.5	5.9	5.9
32	2012	Berceto	67.4	0.098	72.4	5.2	5.0
33	1990	Potenza	29.0	0.096	10.0	5.2	5.8
34	1997	Sellano	4.1	0.082	4.8	5.1	5.2
35	1978	Bruzzano Zeffirio	9.2	0.076	5.0	5.3	5.2
36	2004	Vobarno	13.6	0.072	5.4	5.2	5.0
37	2012	Mirabello	20.4	0.070	3.4	5.1	5.2
38	2002	Bonefro	38.1	0.057	13.0	5.4	5.7
39	2018	Molise	22.3	0.045	19.6	5.2	5.1
40	2002	Casacalenda	46.1	0.032	10.0	5.3	5.7
41	2008	Neviano degli Arduini	47.6	0.022	22.9	5.2	5.5